ROYAL SOCIETY
OF CHEMISTRY

PCCP

ARTICLE

Ultrafast photoisomerisation of an isolated retinoid

James N. Bull,[a,†] Christopher W. West,[b] Cate S. Anstöter,[c] Gabriel da Silva,[d] Evan J. Bieske,[e] Jan R. R. Verlet[c]

The photoinduced excited state dynamics of gas-phase *trans*-retinoate (deprotonated *trans*-retinoic acid, *trans*-RA⁻) are studied using tandem ion mobility spectrometry coupled with laser spectroscopy, and frequency-, angle- and time-resolved photoelectron imaging. Photoexcitation of the bright $S_3(\pi\pi^*) \leftarrow S_0$ transition leads to internal conversion to the $S_1(\pi\pi^*)$ state on a ≈80 fs timescale followed by recovery of S_0 and concomitant isomerisation to give the 13-*cis* (major) and 9-*cis* (minor) photoisomers on a ≈180 fs timescale. The sub-200-fs stereoselective photoisomerisation parallels that for the retinal protonated Schiff base chromophore in bacteriorhodopsin. Measurements on *trans*-RA⁻ in methanol using the solution photoisomerisation action spectroscopy method shows that 13-*cis*-RA⁻ is also the principal photoisomer, although photoisomerisation is roughly six times slower than in the gas phase. Furthermore, the 13-*cis* and 9-*cis* photoisomers are formed with an inverted branching ratio with photon energy in methanol when compared with the gas phase, presumably due to solvent-induced modification of potential energy surfaces and inhibition of electron detachment processes. This work provides clear experimental evidence that solvation significantly affects the photoisomerisation dynamics of retinoid molecules.

Introduction

There are several families of seven-transmembrane retinal proteins found throughout the biological kingdoms that use light to trigger activity.[1-4] These include visual rhodopsins (photoreceptor in vision), bacteriorhodopsins and proteorhodopsins (proton pumps), halorhodopsin (anion pump), channelrhodopsin (ion channels), and other sensory rhodopsins (phototaxis receptors). In all cases the photoreceptor is a derivatised retinal molecule that undergoes a sub-picosecond isomerisation (sub-200 fs for visual rhodopsin and bacteriorhodopsin),[5-11] which is amongst the fastest chemical transformations in biology. Photoisomerisation occurs stereoselectively about one of the chromophore's five double bonds with a quantum yield of up to 0.65.[12, 13] For example, in visual rhodopsin the absorption of visible light by retinal protonated Schiff base (RPSB) triggers an 11-*cis* → *trans* isomerisation, while a *trans* → 13-*cis* isomerisation occurs in bacteriorhodopsin. Theory and experiment have firmly established that these isomerisations involve passage through a S_1/S_0 conical intersection at a geometry intermediate between a *trans* and *cis* configuration.[8, 14-16] In two recent

studies on bacteriorhodopsin, time-resolved X-ray Laue and serial crystallography experiments with near atomic resolution were able to monitor the ultrafast structural evolution of the chromophore and host protein following the absorption of light,[17, 18] suggesting that the *trans* → 13-*cis* stereospecificity and high quantum yield stem from specific interactions between the chromophore and amino acid residues within the protein's binding pocket. To help unravel the importance of intermolecular and intramolecular factors that influence the photoisomerisation dynamics, it is important to understand the inherent photophysics of the isolated chromophore. In this context, gas-phase studies allow the chromophore to be probed in an environment free from intermolecular interactions and allow straight-forward comparison with theory. Here, we present a comprehensive study of the excited state dynamics of a prototype gas-phase retinoid chromophore, deprotonated *trans*-retinoic acid (*trans*-RA⁻, Fig. 1). We show that an ultrafast and stereoselective photoisomerisation occurs for *trans*-RA⁻ despite the absence of protein side-group interactions, and these dynamics are strongly affected by solvation.

The desire to understand the photoisomerisation dynamics of retinal chromophores has prompted numerous studies of RPSB and other retinal molecules in solution, including primary retinoids such as retinol and retinoic acid (vitamin A series). Several of the primary retinoids are biological precursors to RPSB,[19, 20] and have important light harvesting roles with protein-binding chromophores such as chlorophyll and bacteriochlorophyll, for photoprotecting mechanisms in orange carotenoid protein, and as hormones for epithelial cell growth and development.[21-23] Whereas the photoactive state of RPSB is the bright $S_1(^1\pi\pi^*)$ state, the primary retinoids resemble the *beta*-carotenes in which the first $^1\pi\pi^*$ [A_g] and $^1n\pi^*$ states are dark and the second $^1\pi\pi^*$ [B_u^+] state is optically bright. Selected RPSB isomers in solution exhibit lower photoisomerisation quantum yields and longer photoisomerisation timescales than when in a protein environment.[24-26] For example, the photoisomerisation quantum yield of *trans*-RPSB in hexane (product isomer distribution in parentheses) is 0.14 (1.7:4.6:1.0 ratio of 13-*cis*:11-*cis*:9-*cis*) and 0.13 (1.9:3.7:1.0 ratio of

[a.] School of Chemistry, Norwich Research Park, University of East Anglia, Norwich NR4 7TJ, United Kingdom
Department of Chemistry, Graduate School of Science, Kyoto University, Kitashirakawa Oiwake-cho, Sakyo-Ku, Kyoto 606-8502, Japan
Department of Chemistry, Durham University, Durham DH1 3LE, United Kingdom
Department of Chemical Engineering, University of Melbourne, Parkville, VIC 3010, Australia.
School of Chemistry, University of Melbourne, Parkville, VIC 3010, Australia.
† Corresponding author. Email: james.bull@uea.ac.uk
Electronic Supplementary Information (ESI) available: ATDs with collisional excitation, Photoaction ATDs with light fluence, Solution absorption spectra, RRKM rates, 3.10 + 1.55 eV time-resolved data; Time-resolved spectra fitting procedure, CASSCF natural orbitals, SPISA spectroscopy light fluence. See DOI: 10.1039/x0xx00000x
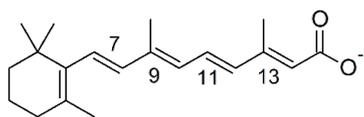
Fig. 1 – Structure of *trans*-RA⁻ (deprotonated *trans*-retinoic acid). Numbers indicate bond positions for the *cis* isomers. The conjugate acid is denoted as *trans*-RAH.

13-*cis*:11-*cis*:9-*cis*) in methanol,[26-28] compared with 0.65 in bacteriorhodopsin. Furthermore, the $S_1(\pi\pi^*)$ state of *trans*-RPSB survives for ≈30 ps in hexane and ≈4 ps in methanol,[29-31] which is two to three orders of magnitude longer than in bacteriorhodopsin. For *trans*-retinoic acid (*trans*-RAH) in solution, $S_3(\pi\pi^*) \rightarrow S_1(\pi\pi^*)$ internal conversion occurs on a sub-100 fs timescale while the $S_1(\pi\pi^*)$ state can survive for 1 to 55 ps depending on the solvent viscosity and polarity.[32-37] For RPSB in solution, variations in photoisomerisation quantum yield, product branching ratio and excited state lifetime with solvent are due to several factors, including frictional effects of solvent molecules, solvent-induced modification of the potential energy surfaces, and vibrational energy quenching.[24, 26, 38-45] It is thought that the combination of these effects causes the photoexcited population to become temporarily trapped behind a barrier on the $S_1(\pi\pi^*)$ potential energy surface, slowing the passage through an isomerising conical intersection.

Although studies on retinoids in solution are informative, they confirm that solvation influences the intrinsic photophysics. Efforts to disentangle the solvent/environmental effects from the intrinsic dynamics has prompted several gas-phase experiments. The first of these combined electrospray ionisation of RPSB with photodissociation spectroscopy, with the photodissociation action spectrum serving as a proxy for the absorption spectrum.[46-48] These measurements were subsequently compared with electronic structure calculations.[49] In a step towards directly observing photoisomerisation in the gas phase, tandem ion mobility spectrometry (IMS) was combined with laser spectroscopy was used to measure a photoisomerisation action (PISA) spectrum for a mixture of isomers and for mobility-selected *trans*-RPSB.[50, 51] In PISA spectroscopy, the target isomer is selected in a primary IMS stage and then exposed to wavelength tuneable light, with the photoisomers separated in a secondary IMS stage. For mobility-selected *trans*-RPSB, PISA spectroscopy confirmed that photoisomerisation occurs in the gas-phase, although the studies were unable to clearly distinguish and assign the photoisomers nor expose details of the photoisomerisation dynamics. In a recent development, a femtosecond pump-probe photodissociation strategy was applied to study the $S_1(\pi\pi^*)$ state of RPSB isomers.[52] The measurements at 300 K were interpreted in terms of two lifetimes, ≈400 fs and ≈3 ps, which were assigned to the 11-*cis* and *trans* isomers, respectively, although the isomer distribution of the electrosprayed population was unclear.

The present study considers the excited state dynamics of gas-phase *trans*-RA⁻ using two complementary techniques: PISA spectroscopy to discriminate the target isomer and probe the photoisomerisation products and their branching ratio, and photoelectron spectroscopy to probe the electron detachment properties and timescale for photoisomerisation. The *trans*-RA⁻ chromophore is an appealing target because: (i) the high thermal stability of the *trans* and *cis* isomers, due to large ground state isomerisation barriers, means the electrosprayed isomeric form is retained and only the primary photoisomerisation response is observed using the PISA spectroscopy technique;[53] (ii) the dynamics of gaseous anions can be readily probed using two-colour femtosecond photoelectron spectroscopy;[54] (iii) photoexcited *trans*-RAH (i.e. the neutral) in non-polar solvents has a negligible intersystem crossing yield and no internal conversion to the $S_2(n\pi^*)$ state,[37] allowing for simpler comparison between the molecules' dynamics in the gas phase and in solution (provided *trans*-RAH and

trans-RA⁻ behave in similar fashions). For gas-phase *trans*-RA⁻, this study provides the first determination of an excitation-energy-dependent branching ratio between the primary photoisomers (13-*cis* + 11-*cis* and 9-*cis*) and direct measurement of the timescale for both $S_3(\pi\pi^*) \rightarrow S_1(\pi\pi^*)$ internal conversion and ensuing isomerisation. These measurements should serve as a benchmark for researchers seeking to understand the influence of a condensed phase environment on the photoisomerisation dynamics of a retinoid.

Methods

A. Ion mobility mass spectrometry

The tandem IMS used in this study has been discussed in elsewhere.[55] The instrument has a custom IMS-photo-IMS-QMF configuration, consisting of two drift regions (IMS1 and IMS2) followed by a quadrupole mass filter (QMF). In an experiment, gas-phase RA⁻ was produced through electrospray (−3 kV) of a ≈20 μmol L⁻¹ methanol solution of either *trans*-RAH, 9-*cis*-RAH or 13-*cis*-RAH (>99 % from Sigma-Aldrich, shielded from light) with a trace of ammonia. Electrosprayed anions were transferred *via* a heated capillary into a radio frequency (RF) ion funnel, which radially gathered and confined the ions. A pulsed ion gate (IG1, ≈100 μs opening time) at the end of the ion funnel injected packets of ions at 40 Hz into IMS1. In the drift region, the ions were propelled by an electric field (44 V cm⁻¹) through N_2 buffer gas at a pressure of ≈6 Torr. More extended ions (*trans* isomers) have larger collision cross-sections than compact ions (*cis* isomers), resulting in longer drift times. In a parallel set of measurements, ≈1% propan-2-ol was seeded into N_2 buffer gas, which, due to isomer-specific ion-molecule interactions, enhanced separation of the *cis* isomers.[56] After ions traversed the entire drift region (IMS1 + IMS2) a second ion funnel collected and introduced them into a differentially pumped octupole ion guide and QMF that mass-selected the ions before they reached a Channeltron ion detector. The detector was connected to a multichannel scaler that produced a histogram of ion counts against arrival time, t, corresponding to an arrival time distribution (ATD). The mobility resolution, $t/\Delta t$, where t is the peak arrival time and Δt is the full-width-half-maximum of the ATD peak, is typically 80−90 for singly-charged anions present in a single isomeric form.[55] In all presented ATDs, $t = 0$ corresponds to the opening of IG1.

For the PISA spectroscopy measurements, packets of ions with similar collision cross-sections were selected using a Bradbury-Nielsen ion gate situated between IMS1 and IMS2 (≈100 μs opening time). Immediately after gating, the ions were excited with a pulse of light from an optical parametric oscillator (OPO, EKSPLA NT342B, <0.4 mJ cm⁻² pulse⁻¹). Higher light fluences apparently produced *dicis* isomers from photon cycling, i.e. multiple absorption and isomerisation/ground state recovery cycles within the ≈5 ns light pulse duration (see ESI). The OPO was operated at 20 Hz, half the rate of ion injection, allowing accumulation of light-on and light-off ATDs. The difference between these ATDs (photoaction ATD) provide the photoresponse. PISA spectra were derived by plotting the photoisomer signal, normalised by light pulse fluence and light-off ion signal, against photon energy.

Collision cross-sections in N_2 buffer gas (Ω_m) for the *trans*, 13-*cis* and 9-*cis*-RA⁻ isomers were measured using the procedure detailed in Ref. [57]. Absolute errors in Ω_m are ±10 Å² and relative errors, e.g. the difference between Ω_m for 13-*cis*-RA⁻ and 9-*cis*-RA⁻, are much smaller (±1 Å²).

It is worth noting that the collision rate in drift region (≈6 Torr) is ≈10^9 s⁻¹. Rapid processes, including prompt electron detachment and isomerisation by passage through a conical intersection, may occur, however slower processes (<10^7 s⁻¹) should be supressed because of

collisional energy quenching. The latter include statistical isomerisation or dissociation on the ground state potential energy surface, and thermionic emission (ground state statistical electron ejection).[53, 56]

ii. Solution photoisomerisation action spectroscopy

Solution photoisomerisation action (SPISA) spectroscopy on *trans*-RA⁻ used the ion mobility instrument described above and the SPISA procedure detailed elsewhere.[58] Briefly, a ≈20 μmol L⁻¹ solution of sample dissolved in methanol (10 mL) and adjusted to pH ≈11 using several drops of 30% aqueous ammonia was loaded into a syringe that was protected from light and connected *via* a 300 mm section of ETFE capillary (0.50 mm bore, flow rate 20 μL min⁻¹) to the electrospray ion source. ETFE has near uniform optical transparency over the target photoexcitation window (2.8 – 4.1 eV). At pH ≈11, >99.9% of retinoic acid molecules are deprotonated (*trans*-RA⁻). Ions in solution were photoactivated by irradiating a ≈5 mm section of the capillary immediately before its connection to the electrospray source using light from an OPO (EKSPLA NT342B, 20 Hz, unfocused). ATDs were recorded at each photon energy using a light fluence that was attenuated to achieve an isomerisation response of no more than a few percent to avoid sequential photoisomerisations (e.g. *trans* → *cis* → *dicis*, see ESI). The SPISA spectra were derived by plotting photoisomer yield normalised by total electrospray signal and light fluence against photon energy.

B. Photoelectron spectroscopy
i. Frequency- and angle-resolved photoelectron imaging

The photoelectron imaging apparatus and frequency-, angle- and time-resolved photoelectron imaging methodology has been described elsewhere.[54, 59] Briefly, *trans*-RA⁻ was produced through electrospray (−5 kV) of a ≈1 μmol L⁻¹ solution of *trans*-RAH (99 % from Sigma-Aldrich, shielded from light) in methanol with a trace of ammonia. Electrosprayed ions were introduced into a RF ring-electrode ion trap using a vacuum transfer capillary. The RF drive voltage applied to the ion trap was kept low to minimise collisional isomerisation of the ions. The trapped ions were unloaded (50 Hz) into a colinear time-of-flight ion optics assembly that accelerated them along a 1.3 m flight region toward a continuous-mode penetrating field velocity-mapping assembly.[59] Laser pulses were timed to interact with the mass-selected *trans*-RA⁻ ion packet in the centre of the velocity-map imaging stack. Ejected electrons were velocity mapped onto a dual (chevron) multichannel plate (MCP) and P43 phosphor screen detector that was monitored with a charge-coupled device (CCD) camera. All CCD images were accumulated with a 500 ns MCP detector gate. The velocity-mapping resolution was ≈5%. The electron kinetic energy (eKE) scale was calibrated from the photoelectron spectrum of I⁻. Velocity-map image reconstructions used a polar onion peeling algorithm,[60] providing the photoelectron spectra and associated angular distributions in terms of β_2.[61] β_2 values range between −1 and 2, corresponding to electron ejection perpendicular and parallel to the laser polarisation axis, respectively.

For the frequency-resolved photoelectron imaging, pulses of light were derived from an OPO (Continuum Horizon) pumped by a Nd:YAG laser (Continuum Surelite II). Light pulse fluence of < 0.2 mJ (≈5 mm² beam cross section) was required to minimise broadening of the low-eKE feature (from photon cycling) in the 3.10 eV photoelectron spectrum. Comparison of the 3.10 eV photoelectron spectra recorded using nanosecond and femtosecond laser light confirmed minimal photon cycling in the frequency-resolved measurements. In another set of measurements, prompt *vs* delayed features in the 3.10 eV spectrum were investigated by delaying the acquisition gate on the MCP detector relative to the light pulse.[62] For example, a measurement using an acquisition gate delay of 50 ns

showed some fraction of the low-*eKE* signal occurred on a >50 ns timescale, consistent with a contribution from thermionic emission.

ii. Time-resolved photoelectron imaging

For the time-resolved experiments, femtosecond light pulses were derived from a commercial Ti:sapphire oscillator and regenerative amplifier (Spectra-Physics). The 3.10 eV (400 nm, ≈30 μJ) pump pulses were produced by frequency doubling the fundamental output with a type II β-barium borate crystal. Two probe regimes were used: (i) 2.49 eV (500 nm, ≈50 μJ) and (ii) 1.55 eV (800 nm, ≈200 μJ). The 2.49 eV probe was produced by sum-frequency mixing the fundamental output with the signal output from an optical parametric amplifier (Light Conversion TOPAS-C). The pump and probe pulse energies where chosen to avoid multiphoton detachment in single-colour images (large radius rings in the velocity-map images). The pulses were delayed relative to each other (Δt) using a motorised delay line, combined collinearly using a dichroic mirror, and loosely focused into the interaction region (beam cross-section ≈4 mm²) using a curved metal mirror. The pump-probe cross correlation was ≈70 fs (2.49 eV probe) and ≈50 fs (1.55 eV probe).

C. Computational
i. Isomer energies and potential energy surfaces

Electronic structure calculations were performed using the Firefly 8.2.0, ORCA 4.0.1 and Gaussian 16 software packages.[63-65] Structures of the *trans*, *cis* and selected *dicis* isomers were computed at the BH&HLYP/aug-cc-pVDZ level of theory and confirmed as geometrical minima through vibrational frequency analysis.[66, 67] Single-point energy calculations were then performed at the DLPNO-CCSD(T)/aug-cc-pVDZ level of theory.[68] Optimised geometries and isomerisation transition states were consistent with an earlier conformation study, which concluded that the equilibrium structures for the *trans*, 13-*cis* and 9-*cis* isomers have s-*gauche* configurations of the β-ionone ring and *trans* has a ≈53˚ dihedral angle between the ring and polyene tail.[69, 70]

Vertical excitation energies were calculated at the multi-state XMCQDPT2 method with CASSCF(16,13)/GEN or CASSCF(12,11)/GEN reference wavefunctions and the MP2/GEN optimized geometry.[71] The (16,13) active space included five π, three *n* orbitals [O(p)] and five π* orbitals – see ESI for further details. The (12,11) active space excluded the two lowest energy *n* orbitals (not important for the vertical excitation energy of the ¹*n*π* state at the *trans*-RA⁻ geometry). No symmetry constraints were applied. The GEN basis set is the aug-cc-pVDZ basis set excluding the most diffuse set of *d* orbitals for C and O atoms and the cc-pVDZ basis set for H atoms.

ii. Ion mobility collision cross-sections

Collision cross-sections, Ω_c, were calculated using MOBCAL with the trajectory method parametrised for N_2 buffer gas using input charge distributions (BH&HLYP/aug-cc-pVDZ level of theory) from the Merz-Singh-Kollman scheme constrained to reproduce the molecule's electric dipole moment.[72, 73] Sufficient trajectories were computed to give standard deviations of ±1 Å² for the calculated values. Note that MOBCAL was parameterised for cations and its performance for anions has not been benchmarked.

iii. RRKM theory statistical modelling

RRKM theory calculations using the MultiWell suite of programs[74] were carried out to characterise the microscopic rates on the ground electronic state, $k_{A\rightarrow B}(E)$ where A is the parent isomer (*trans*), B is a
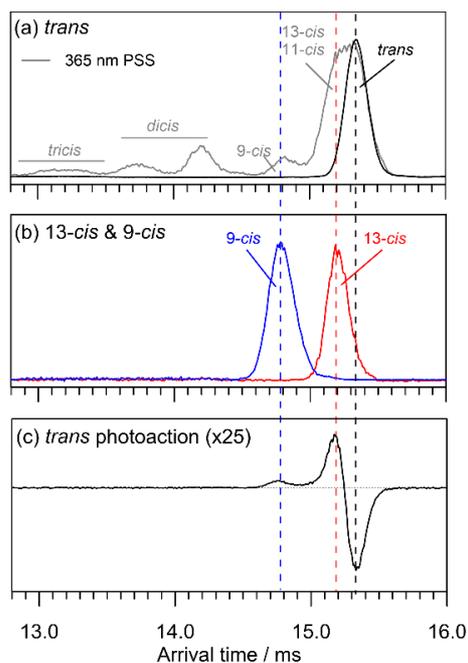
Fig. 2 – ATDs for selected isomers of RA⁻ in N₂ buffer gas: (a) *trans* isomer and a photostationary state (PSS) in which a methanolic solution was irradiated with light from a UV LED (385 nm), (b) 13-*cis* and 9-*cis* isomers, (c) *trans* photoaction (light-on – light-off) ATD at 3.49 eV (≈0.4 mJ cm⁻² pulse⁻¹) by intercepting the gas-phase ions with a pulse of light immediately after they were injected into IMS1. The total depletion signal in (c) exceeds photoisomer appearance signal, presumably due to electron detachment.

single-*cis* isomer and E is the total vibrational energy. In these calculations, sums and densities of states for ground state minima and transition states were calculated from Stein-Rabinovitch-Beyer-Swinehart counts using the BH&HLYP/aug-cc-pVDZ optimized structures, vibrational frequencies, moments of inertia and zero-point energies. The symmetric top assumption was invoked for external degrees of freedom, while the internal degrees of freedom were described as harmonic oscillators. Electronic energies used the DLPNO-CCSD(T)/aug-cc-pVDZ values.

Results and discussion

A. Ion mobility mass spectrometry

This section details the application of PISA spectroscopy to (i) characterise photoisomerisation of gas-phase *trans*-RA⁻ to the 13-*cis* and 9-*cis* isomers (a small amount of 11-*cis* might be counted as 13-*cis*) with a branching ratio that depends on excitation energy, and (ii) demonstrate that electron detachment competes with isomerisation.

i. Arrival time distributions and photoisomer assignments

ATDs for *trans*-RA⁻, 13-*cis*-RA⁻, and 9-*cis*-RA⁻ using pure N₂ buffer gas and N₂ buffer gas seeded with ≈1% propan-2-ol are shown in Fig. 2 and Fig. 3, respectively. The ATDs show that the *trans*-RA⁻ and 13-*cis*-RA⁻ ATD peaks are slightly separated with N₂ buffer gas but are baseline separated with the N₂ + ≈1% propan-2-ol buffer gas. Conversely, *trans*-RA⁻ and 9-*cis*-RA⁻ ATD peaks are baseline separated with N₂ buffer gas and are partially separated with N₂ + ≈1% propan-2-ol buffer gas. Unfortunately, we were unable to obtain a pure sample of the 11-*cis* and 7-*cis* isomers to measure their ATDs, however, in the following we argue that both are expected to be minor photoisomers.

Photoaction (light-on – light-off) ATDs at 3.49 eV (355 nm, 40 Hz, ≈0.4 mJ cm⁻² pulse⁻¹) in which *trans*-RA⁻ ions were irradiated immediately after their injection into IMS1 are shown in Figs 2(c) and
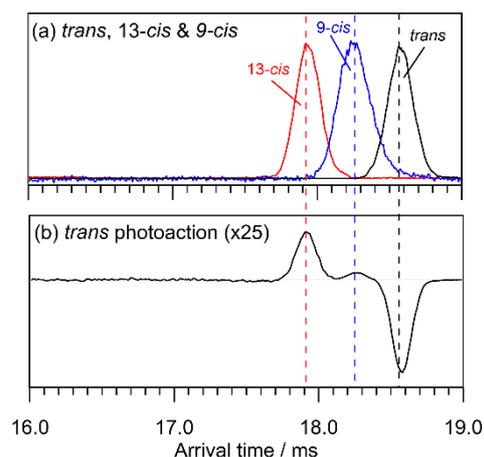

Fig. 3 – ATDs for selected isomers of RA⁻ in N₂ buffer gas seeded with ≈1% propan-2-ol: (a) *trans*,13-*cis* and 9-*cis* isomers, (b) *trans* photoaction (light-on – light-off) ATD at 3.49 eV (≈0.4 mJ cm⁻² pulse⁻¹) by intercepting the gas-phase ions with a pulse of light immediately after they were injected into IMS1. The total depletion signal in (b) exceeds photoisomer appearance signal, presumably due to electron detachment.

3(b). These ATDs suggest two photoisomers are formed with ATD peak arrival times consistent with their assignment as 13-*cis*-RA⁻ and 9-*cis*-RA⁻. As explained later, a small amount of 11-*cis* might be counted as 13-*cis*. Photoaction ATDs recorded with higher light fluences showed substantial yields of more compact isomers, assigned to *multicis* isomers formed through sequential absorption processes (e.g. *trans* → 13-*cis* → *dicis*, see ESI).

A photostationary state (PSS) ATD is shown in Fig. 2(a) in which a methanolic solution of *trans*-RAH (without pH adjustment) was irradiated with light from a 385 nm (20 nm bandwidth) LED immediately before being electrosprayed.[75] The purpose of this measurement was to compare PSS ATD peak areas with isomer abundances determined by HPLC and to further confirm the photoaction ATD peak assignments. The PSS ATD exhibits peaks consistent with the 13-*cis* (major single-*cis*) and 9-*cis* (minor single-*cis*) photoisomers and several more compact isomers tentatively assigned as 13,11-*dicis*, 13,9-*dicis* and 13,11,9-*tricis* isomers through comparison with the HPLC measurements.[76-79] The HPLC measurements suggested an 11-*cis* yield slightly less than that of 9-*cis* and no 7-*cis*, consistent with 11-*cis* being counted as 13-*cis* and 7-*cis* having no contribution to the PSS or photoaction ATDs.

Calculations of the RA⁻ isomers (Table 1) show that *trans*-RA⁻ is

Species	E / eV	TS / eV	Ω_c / Å²	Ω_m / Å²
trans	0.00	-	206	200
13-*cis*	0.04	2.05	204	198
11-*cis*	0.22	1.53	204	-
9-*cis*	0.06	1.49	203	193
12-*cis*	0.18	0.37	205	-
10-*cis*	0.19	0.32	204	-
8-*cis*	0.10	0.34	206	-
7-*cis*	0.30	-[a]	201	-
13,11-*dicis*	0.44	-	202	-
13,9-*dicis*	0.25	-	202	-
13,11,9-*tricis*	0.48	-	203	-

Table 1 – Isomer and transition state (TS) energies at the DLPNO-CCSD(T)/aug-cc-pVDZ level of theory relative to *trans*-RA⁻, and calculated (Ω_c) and measured (Ω_m) collision cross-sections in N₂ buffer gas. Only *dicis*/*tricis* isomers identified in reference HPLC measurements are given. Note: 1 eV = 96.486 kJ mol⁻¹. [a]The 7-*cis* TS barrier is >2 eV and difficult to optimise due to steric interactions.

the lowest energy form, followed by 13-*cis*-RA$^-$ and then 9-*cis*-RA$^-$. Calculated collision cross-sections in N$_2$ buffer gas (Ω_c in Table 1) are consistent with the measured values: Ω_m(*trans*-RA$^-$) > Ω_m(13-*cis*-RA$^-$) > Ω_m(9-*cis*-RA$^-$). Note that the Ω_c values assume the minimum energy geometry for each isomer and do not account for rotamers or fluxionality of the ions in the drift region. Differences between the Ω_c and Ω_m values are most likely due to neglect of rotamers when calculating Ω_c and the approximate nature of the intermolecular potential energy functions assumed in MOBCAL. The energies listed in Table 1 suggest that the 11-*cis* and 7-*cis* isomers lie substantially higher in energy than the 13-*cis* or 9-*cis* isomers, implying they are less likely to be formed through statistical processes in the gas phase (e.g. collisional). However, the Ω_c values indicate that the 11-*cis* ATD peak may overlap the 13-*cis* ATD peak in pure N$_2$ buffer gas. Furthermore, because there was no evidence for additional peaks in the photoaction ATDs recorded using N$_2$ + ≈1% propan-2-ol buffer gas and low light fluence, we conclude that 11-*cis* is either not formed or is not resolved from 13-*cis*.

Calculations of transition states for interconversion between *trans* and the various single-*cis* isomers (Table 1) indicate that internal rotation about 'double' bonds have large (>1.5 eV) rotation barriers, whereas the internal rotation barriers about 'single' bond barriers are appreciably smaller than the average thermal energy of the ions in the drift region (≈0.56 eV from harmonic partition function at 298 K), suggesting the even-numbered isomers can be considered as rotamers that will rapidly interconvert between *E* and *Z* forms in the drift region (see RRKM calculations below). The calculated internal rotation barriers about 'single' bonds are consistent with an earlier theoretical study on the conformational space of *trans*-RA$^-$ and 9-*cis*-RA$^-$.[70]

ii. Photoisomerisation action spectroscopy

With the above photoisomer assignments, we recorded PISA spectra for mobility-selected *trans*-RA$^-$, monitoring formation of the 13-*cis* and 9-*cis* photoisomers as a function of photon energy [Fig. 4(a)]. These spectra were obtained through measurements using N$_2$ buffer gas (high ion throughput, good separation of 9-*cis* and *trans*) and N$_2$ + ≈1% propan-2-ol buffer gas (low ion throughput, good separation of 13-*cis* and *trans*) and fitting both photoaction ATD sets with a global model. The global fit assumed each ATD peak was described by a Gaussian function with peak arrival time and width parameters averaged across all photoaction ATDs for a given buffer gas.[56] The global fit required the relative area of each Gaussian peak at a given photon energy to be equal in both buffer gases, i.e. the relative yields of the photoisomers and for photodetachment are the same in both buffer gases.

The PISA spectra in Fig. 4(a) show that photoisomerisation occurs over the 2.7 – 4.4 eV range, producing 13-*cis* as the main photoisomer with maximum response at 3.7 eV. The 9-*cis* isomer is produced over the same photon energy range but with a different photon energy dependence with the maximum response occurring ≈0.2 eV higher at 3.9 eV. The 9-*cis*:13-*cis* branching ratio is plotted against photon energy in Fig. 4(b). It is worth noting again that there was no evidence for formation of *dicis* or *tricis* photoisomers at any photon energy (2.7 – 4.4 eV) at low light fluence (<0.4 mJ cm^{-2} pulse^{-1}), suggesting that absorption of one photon causes isomerisation about one double bond.

The photoaction ATDs [Figs. 2(c) and 3(b)] show net depletion of the ions, i.e. the photodepletion signal exceeds the photoisomer appearance signal. The difference is attributed to electron detachment because no fragment ions (e.g. decarboxylation) were detected when the QMF was operated as an ion guide (no mass filtering), and is also consistent with the photoelectron spectroscopy measurements presented in the next section. Although the instrument has low transmission for ions with *m/z* < 80, decarboxylation is usually the
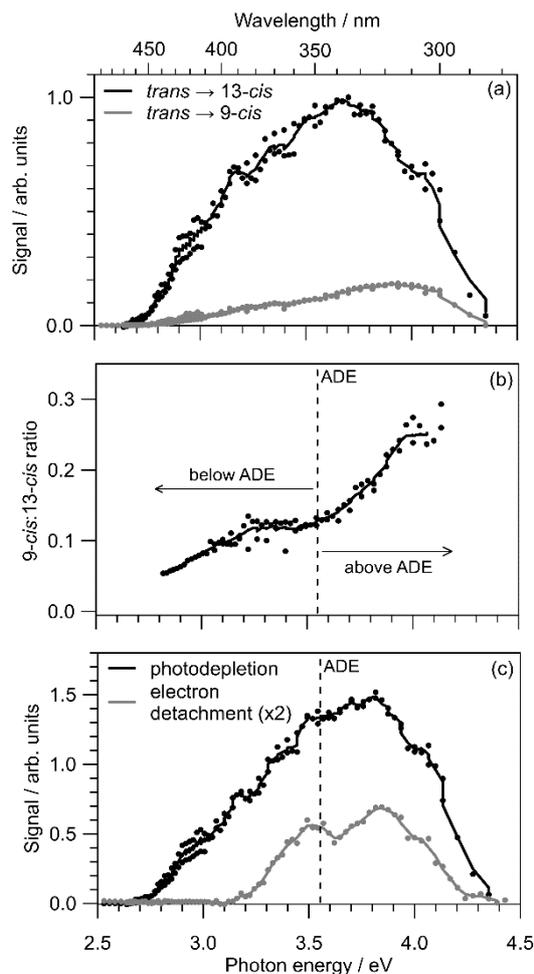

Fig. 4 – Photoisomerisation of gas-phase *trans*-RA$^-$: (a) *trans* → 13-*cis* and *trans* → 9-*cis* spectra, (b) 9-*cis*:13-*cis* photoisomer ratio with photon energy, and (c) photodepletion and electron detachment ('total depletion' – 'total PISA') spectra. Note, in (a) and (b), a small contribution from the 11-*cis* isomer may be counted as 13-*cis*. The electron detachment spectrum has an onset ≈0.5 eV below the ADE due to the initial thermal energy of the ions. ADE is the adiabatic detachment energy at 3.55±0.05 eV (see Section B).

main fragmentation pathway for deprotonated carboxylic acids.[80] Photodepletion and electron detachment action spectra are shown in Fig. 4(c). The electron detachment yield has a bimodal distribution. If real, this might be due to competition between electron detachment and internal conversion, with relative yields that depend on excitation energy. The photoisomerisation:photodepletion ratio varies between 1.0 (low photon energy) and 0.7 (high photon energy) and is ≈0.79 at 3.7 eV (maximum of the PISA spectrum). At low photon energy (below the adiabatic detachment energy [ADE]) the ions are unlikely to gain enough energy to detach an electron, explaining the preponderance of photoisomerisation. At this stage it is unclear whether the total photodepletion action spectrum mirrors the absorption spectrum because processes such internal conversion or fluorescence do not necessarily lead to loss of the *trans*-RA$^-$ ions.

Transition	(16,13)	(12,11)	f
S$_1$($\pi\pi^*$) ← S$_0$	1.76	1.83	0.006
S$_2$($n\pi^*$) ← S$_0$	3.33	3.39	0.001
S$_3$($\pi\pi^*$) ← S$_0$	4.05	4.05	1.65

Table 2 – Vertical excitation energies in eV at the MS-XMCQDPT2/GEN (MP2/GEN geometry) with the (16,13) or (12,11) active space. f are CAS-CI oscillator strengths.
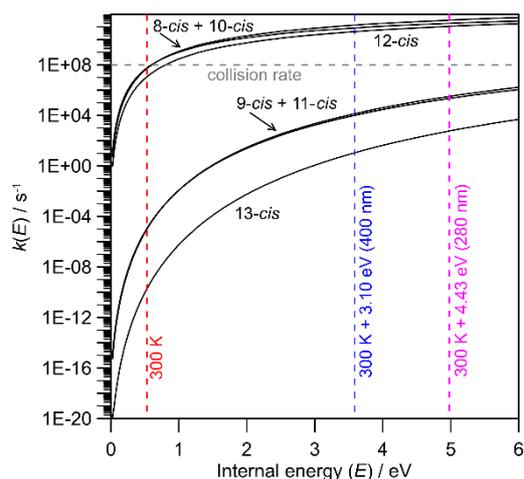
Fig. 5 – RRKM theory rates, $k(E)$, for statistical isomerisation of *trans*-RA⁻. Vertical dashed lines correspond to the initial thermal energy of the ions at 300 K (red, 0.56 eV), plus the energy imparted by a 3.10 eV (400 nm, blue) or 4.43 eV (280 nm, violet) photon. Note the log scale for $k(E)$. $k(E)$ values for the reverse single-*cis* → *trans* isomerisations are given in the ESI.

Calculated vertical excitation energies for *trans*-RA⁻ are given in Table 2 (see orbitals in the ESI). The $S_1(\pi\pi^*) \leftarrow S_0$ transition has $\pi\pi^*$ character and correlates with the symmetry forbidden A_g state in other primary retinoids. The $S_2 \leftarrow S_0$ transition has $n\pi^*$ character involving an oxygen p orbital on the carboxylate group. The $S_3(\pi\pi^*) \leftarrow S_0$ transition corresponds to the second $\pi\pi^*$ state and correlates with the bright B_u^+ state in other primary retinoids. The calculated vertical excitation energy for the $S_3(\pi\pi^*) \leftarrow S_0$ transition at 4.05 eV overestimates the maximum response in either the *trans* → 13-*cis* or total (*trans* → 13-*cis* + 9-*cis*) PISA spectra [both 3.7 eV, Fig. 4(a)] and the photodepletion spectrum [3.85 eV, Fig. 4(c)].

iii. Photoisomerisation mechanism

Photoinduced isomerisation can proceed *via* two mechanisms: (i) direct, ultrafast photoisomerisation by passage of an excited state molecule through a conical intersection seam at a geometry intermediate between *trans* and a single-*cis* isomer, or (ii) recovery of energised *trans*-RA⁻ ions in the ground electronic state, which subsequently undergo statistical isomerisation by traversing isomerisation barriers (transition states).[53] The relatively high pressure of the drift region ($\approx$6 Torr) means that photoactivated ions must isomerise before they collisionally cool. To ascertain the importance of mechanism (ii), we used RRKM theory to calculate isomerisation rates $k(E)$ for total vibrational energy E. Values of $k(E)$ for *trans*-RA⁻ → *cis*-RA⁻ transformations are shown in Fig. 5. Because the collision rate in the drift region is $\approx$10⁹ s⁻¹ and tens to hundreds of collisions are required to thermalise photoactivated ions, isomerisations with $k(E) > 10^7$ s⁻¹ could occur by mechanism (ii). Comparing this limit with the $k(E)$ values in Fig. 5 suggests that mechanism (ii) is not important for *trans* to 13-*cis*, 11-*cis* or 9-*cis* isomerisations over the photon energy range used in this study. On the other hand, the $k(E)$ values suggest that internal rotation about the 12-*cis*, 10-*cis* and 8-*cis* bonds occurs on a timescale that is short compared to the drift time ($\approx$15.3 ms for *trans*-RA⁻ in N₂) and the corresponding rotamers will not be resolved in the ATDs. Therefore, ATD peaks for the *trans*, 13-*cis* and 9-*cis* isomers will represent contributions from all single bond rotamers.[81] Ultimately, these RRKM calculations suggest that the photoisomer yields in Fig. 4(a) are due to photoisomerisation by passage through a conical intersection rather than statistical isomerisation on the ground electronic state.

B. Photoelectron spectroscopy

This section details the application of the frequency-, angle and time-resolved photoelectron imaging methodology to study the excited state dynamics in *trans*-RA⁻. The frequency- and angle-resolved photoelectron imaging technique involves recording a series of velocity-map images with varying photon energy and examining trends across the photoelectron spectra and photoelectron angular distributions. These measurements suggest there are at least three electron detachment channels. Time-resolved measurements at the pump photon energy of 3.10 eV provide information on the excited state dynamics following excitation of $S_3(\pi\pi^*)$ state.

i. Frequency- and angle-resolved photoelectron imaging

The frequency-resolved photoelectron spectrum for *trans*-RA⁻ [Fig. 6(a)] consists of 27 area-normalised photoelectron spectra. Two example spectra are shown in the inset. Photoelectron angular distributions associated with the frequency-resolved spectrum, which are characterised in terms of β_2 values, are shown in Fig. 6(b). A non-zero β_2 implies electron detachment is fast compared with molecular rotation (picoseconds).

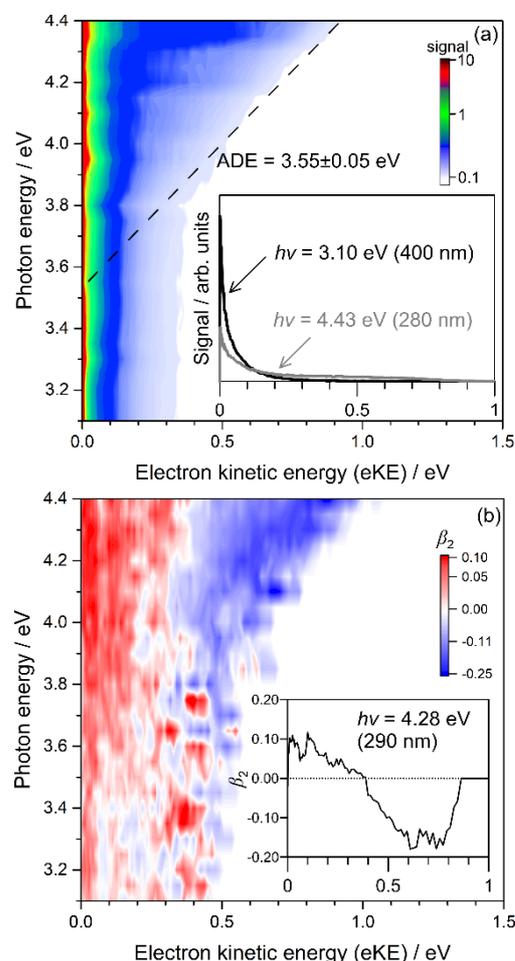The frequency-resolved spectrum in Fig. 6(a) provides the adiabatic detachment energy (ADE) for *trans*-RA⁻ as 3.55±0.05 eV,

Fig. 6 – Frequency-resolved photoelectron spectrum of *trans*-RA⁻: (a) colour map of all 27 photoelectron spectra and two example spectra in the inset, and (b) photoelectron angular distributions (β_2) associated with the frequency-resolved spectrum. β_2 values range -1 to 2, corresponding to electron ejection perpendicular and parallel to the laser polarisation, respectively. Note, there is signal below the ADE due to the initial thermal energy of the ions (vibrational energy of $\approx$0.56 eV at 300 K).

which agrees with the calculated value of 3.54 eV at the DLPNO-CCSD(T)/aug-cc-pVDZ level of theory. Calculated ADE values for the 13-*cis* and 9-*cis* isomers are 3.54 and 3.37 eV, respectively. The experimental vertical detachment energy (VDE) is 3.9±0.1 eV, which agrees with the DLPNO-CCSD(T)/aug-cc-pVDZ value of 4.02 eV.

The frequency-resolved spectrum shows a Boltzmann-like low-eKE feature across all photon energies. Such a feature could result from three processes: (i) autodetachment from a non-valence state, e.g. dipole bound on a picosecond timescale (although such processes often show vibrational structure when using high-resolution velocity-map imaging);[82, 83] (ii) vibrational autodetachment (VAD) from a valence-localised excited electronic state situated below the detachment threshold, e.g. $S_1(\pi\pi^*)$ on a femtosecond to picosecond timescale; (iii) thermionic emission (TE), in which recovery of a vibrationally energised ground electronic state is followed by statistical electron emission occurring on a nanosecond to millisecond timescale.[54] Some contribution from mechanism (iii) is expected since the PISA spectroscopy showed formation of stable photoisomers (which implies recovery of the ground electronic state). The β_2 values associated with the low-eKE feature are positive, which indicates a contribution from detachment processes occurring more rapidly than molecular rotation [mechanisms (i) and (ii)], although mechanism (i) can be ruled out from the time-resolved measurements described in the next section. To test for a contribution from TE in the 3.10 eV spectrum, we recorded the photoelectron spectrum with the MCP imaging gate delayed by 50 ns relative to the light pulse.[62] This spectrum was identical to the original 3.10 eV spectrum shown in the inset in Fig. 6(a), although had $\beta_2 = 0$ (opposed to +0.1 with no gate delay) meaning there is also an isotropic (statistical) electron ejection contribution. We conclude that the low-eKE photoelectron feature is due to some combination of VAD and TE [mechanisms (ii) and (iii)].

In addition to the low-eKE feature, the frequency-resolved spectrum [Fig. 6(a)] has a broad feature in the $3.8 \geq h\nu \geq 4.1$ eV range with a maximum eKE that increases commensurately with photon energy. β_2 values over this photon energy range are non-zero and suggest the involvement of several detachment channels: $\beta_2 = -0.15$ to -0.20 in the $0.5 \leq \mathrm{eKE} \leq 1.0$ eV 'high-eKE' window and $\beta_2 = +0.05$ to $+0.10$ in the $\mathrm{eKE} \leq 0.5$ eV 'low-eKE' window. Signal in the high-eKE window is assigned to prompt detachment,[54, 62, 82] defined as prompt autodetachment from $S_3(\pi\pi^*)$ (i.e. before nuclear reorganisation) and a small amount of direct photodetachment. The difference in β_2 values for the high-eKE and low-eKE windows is consistent with $S_3(\pi\pi^*) \rightarrow S_1(\pi\pi^*)$ internal conversion followed by VAD. This assignment is consistent with the large calculated oscillator strength ($f = 1.65$) for the $S_3(\pi\pi^*) \leftarrow S_0$ transition (Table 2) and with the time-resolved spectroscopy in the next section.

ii. Time-resolved photoelectron imaging

In the time-resolved measurements, a 3.10 eV pump photon accessed the red edge of the *trans*-RA⁻ PISA band [see Fig. 4(a)] while a 2.49 eV or 1.55 eV photon probed the excited state population after time delay, Δt. The effect of the probe in the photoelectron spectra is to translate the eKE distribution associated with the transient excited state population by the probe photon energy. For example, the $S_3(\pi\pi^*)$ state pumped at 3.10 eV and probed at 2.49 eV should have a $\Delta t = 0$ eKE distribution centred at $3.10 + 2.49 - [\mathrm{VDE} = 3.9] \approx 1.7$ eV (0.8 eV for a 1.55 eV probe, see ESI). Time-resolved spectra were determined by subtracting the $\Delta t = -500$ fs spectrum (i.e. probe well before pump) from the $\Delta t \geq -200$ fs spectra; three example time-resolved spectra are shown in Fig. 7(a) (see ESI for examples with the 3.10 + 1.55 eV pump-probe scheme). The time-resolved spectra were interpreted in terms of three pump-probe features: A1 with an eKE window of 1.2 – 2.0 eV which was assigned to the $S_3(\pi\pi^*)$ state since this is the initially-excited state and the pump-probe eKE is
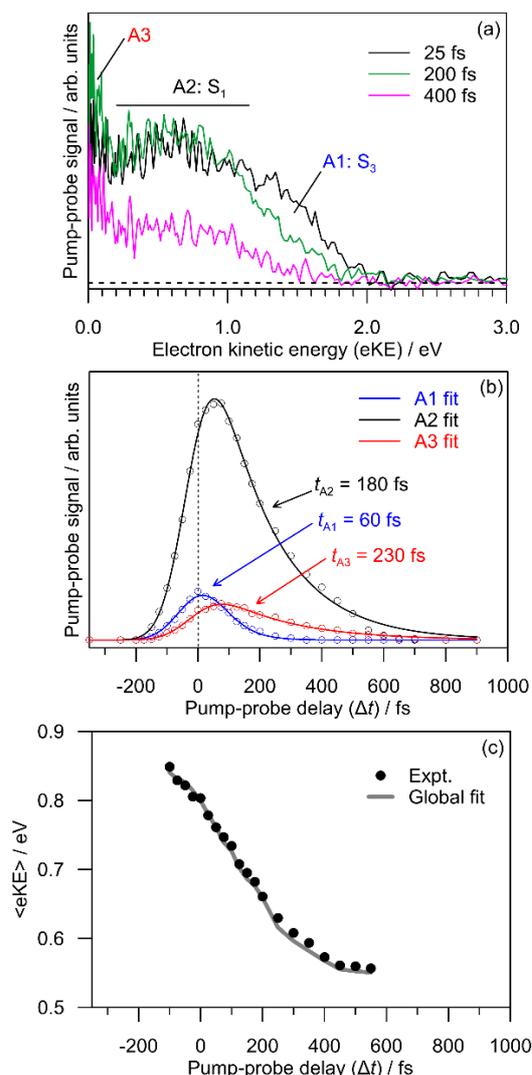

Fig. 7 – 3.10 + 2.49 eV time-resolved photoelectron data for *trans*-RA⁻: (a) three example time-resolved spectra, (b) contributions of each pump-probe feature, and (c) mean time-resolved eKE, <eKE>. The horizontal dashed line in (a) is the zero level. The fitted (Gaussian) cross correlation in (b) is 70±5 fs. A1 is assigned to $S_3(\pi\pi^*) \rightarrow S_1(\pi\pi^*)$ internal conversion, and A2 to $S_1(\pi\pi^*) \rightarrow S_0$ internal conversion and concomitant isomerisation. A3 is tentatively assigned to detachment processes following $S_n \leftarrow S_1(\pi\pi^*)$ (n = 3-5) excitation by the probe. Errors in fitted timescales are ±10 fs. Note, t_{A1} = 80 fs with the 3.10 + 1.55 eV pump-probe scheme (see ESI).

centred around 1.7 eV (see calculation above), A2 with an eKE window of 0.2 – 1.2 eV, and A3 with an eKE window <0.2 eV. The contribution of each pump-probe feature with Δt [Fig. 7(b)] was determined from a global fit of both time-resolved data sets (see ESI). The associated timescales were determined from fits assuming exponential growth/decay functions convoluted with a Gaussian cross-correlation function. The fitted timescales are $t_{A1} = 80$ fs, $t_{A2} = 180$ fs and $t_{A3} = 230$ fs (±10 fs fit errors). Note that the $t_{A1} = 80$ fs value was taken from the 3.10 + 1.55 eV data (see ESI) due to better cross correlation (≈ 50 fs compared with ≈ 70 fs cross correlation for the 3.10 + 2.49 eV scheme).

The decay of time-resolved feature A2 was assigned to $S_1(\pi\pi^*) \rightarrow S_0$ internal conversion with some fraction of concomitant isomerisation by passage through a conical intersection, because: (i) the Δt for maximum signal is delayed by ≈ 75 fs from $\Delta t = 0$ (which is the Δt for maximum contribution from feature A1), suggesting that population associated with A1 transfers into A2; (ii) for the $\Delta t = 0$ to 100 fs time-resolved spectra, the peak in the time-resolved eKE
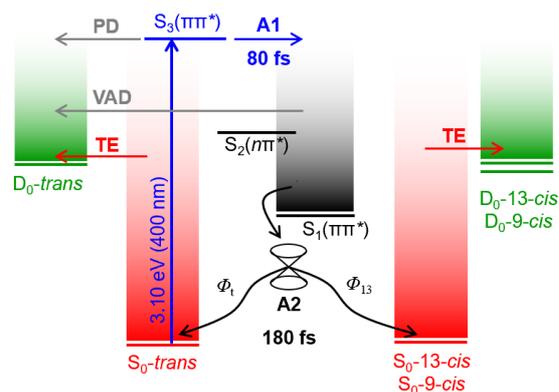
Fig. 8 – Summary of excited state dynamics for *trans*-RA⁻ following excitation of S₃(ππ*) at 3.10 eV (400 nm). S₃(ππ*) → S₁(ππ*) internal conversion (A1) occurs on a ≈80 fs timescale. S₁(ππ*) → S₀ internal conversion (A2) [quantum yield Φ_t] and concomitant isomerisation to 13-*cis* (quantum yield Φ_{13}) and 9-*cis* (quantum yield Φ_9) occurs on a ≈180 fs timescale ($\Phi_9/\Phi_{13} \approx 0.1$ at 3.10 eV). In the high vacuum environment, energised ions in the S₀ state eject the most weakly bound electron on a statistical timescale *via* thermionic emission (TE). Note, $\Phi_t + \Phi_{13} + \Phi_9 < 1$ because of autodetachment and possibly fluorescence. PD is prompt detachment and VAD is vibrational autodetachment.

Fig. 9 – Schematic potential energy surfaces for *trans*-RA⁻ with two photoexcitation schemes, *hv* = 3.1 eV in yellow which gave a 9-*cis*:13-*cis* branching ratio of ≈0.1 and *hv* = 3.8 eV in red which gave a 9-*cis*:13-*cis* branching ratio of ≈0.2. On the S₁(ππ*) surface, the yellow wavepacket has less vibrational energy and might be trapped for a vibration or two before propagating over the barrier and passing through a conical intersection associated with isomerisation. Conical intersection (CI) topography, e.g. peaked *vs* sloped, might also influence the photoisomer distribution. IC indicates internal conversion.

distribution occurs at ≈0.6 eV, suggesting it is associated with an excited state situated at ≈2.0 eV for early time delays, which is consistent with calculated S₁(ππ*)←S₀ vertical excitation energy of ≈1.8 eV (Table 2) for *trans*-RA⁻; (iii) the average pump-probe eKE, <eKE>, in Fig. 7(c) shows that <eKE> decreases with increasing Δ*t*, consistent the probe photon sampling a potential energy surface with large nuclear motion (extensive intramolecular vibrational energy redistribution is improbable on the sub-200 fs timescale[84]); (iv) PISA spectroscopy in Section A demonstrated that photoisomerisation is a predominant process, and RRKM modelling suggested that photoisomer formation was not from statistical isomerisation on the ground electronic state.

Time-resolved feature A3 is more difficult to explain. Specifically, the time-resolved spectra do not show a (negative) photobleach signal which would normally correspond to the final electronic state (i.e. S₀ with a TE distribution in the pump-only spectrum).[54] Assuming time-resolved feature A3 is distinct from A2 (timescales are roughly the same at 180 and 230 fs), a possible explanation is that the probe photon induces a second excitation rather than direct photodetachment. For example, our calculations suggest the Sₙ←S₁(ππ*) ($n = 2 − 5$) transitions have oscillator strengths ranging 0.01 to 0.04 at the initial S₀ geometry. If this hypothesis is correct, the 'pump-pump' population could internally convert back to the S₁(ππ*) state and then autodetach. It follows that the pump-probe photobleach signal would be masked in the background subtraction procedure because the yield of low-eKE electrons from 'pump-pump' autodetachment within the 500 ns MCP imaging gate is greater than the statistical TE contribution (most of which is gated out using a 500 ns imaging gate). Whatever the assignment of time-resolved feature A3, the complete excited state population has decayed within 1 ps, meaning that isomerisation by passage through a conical intersection must occur on the timescale of 180 – 230 fs.

A schematic summary of the time-resolved dynamics is given in Fig. 8, assigning S₃(ππ*)→S₁(ππ*) internal conversion to occur on a ≈80 fs timescale and S₁(ππ*)→S₀ internal conversion with isomerisation to occur on a ≈180 fs timescale.

C. Discussion of gas-phase dynamics

The most striking outcome from the present study is that gas-phase *trans*-RA⁻ undergoes a sub-200-fs stereospecific photoisomerisation.
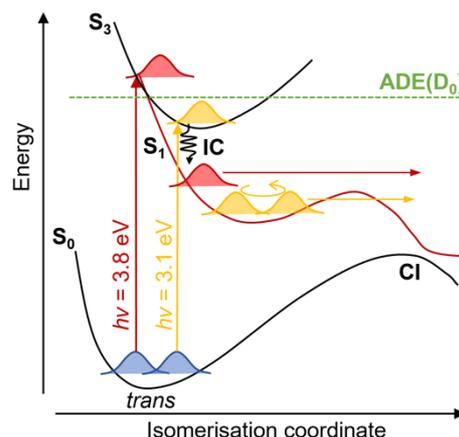
This timescale is similar to that for the *trans*-RPSB → 13-*cis*-RPSB photoisomerisation in bacteriorhodopsin. The timescale is also close to the ≈400 fs excited state lifetime proposed for 11-*cis*-RPSB in a recent gas-phase study (≈3 ps proposed for *trans*-RPSB).[52] Whereas in that study, electrospray ionisation of a given RPSB isomer appeared to produce a distribution of *trans* and *cis* isomers, in this work we show that the *trans*-RA⁻ molecules retain their isomeric form during electrospray ionisation (see ESI for further details). This is presumably due to the higher ground state rotation barriers about the double bonds for *trans*-RA⁻ (Table 1) compared with *trans*-RPSB.[51]

The 13-*cis*:9-*cis* excitation-energy-dependent branching ratio determined in the ion mobility measurements [Fig. 4(b)] is almost certainly due to the topology of the excited state potential energy surfaces. For example, QM/MM modelling[39, 40] of *trans*-RPSB in the gas phase and with methanol solvation suggested that different barriers on the S₁(ππ*) potential energy surface to reach conical intersection seams associated with formation of each photoisomer and different conical intersection topographies,[15, 43, 44] e.g. sloped *vs* peaked, associated with formation of each photoisomer are the two principal factors that influence the photoisomer distribution. In a step toward investigating barriers to isomerisation on the S₁(ππ*) potential energy surface for *trans*-RA⁻, we calculated barrier heights at the MS-XMCQDPT2(12,11)/GEN level of theory by rotating the 13-*cis*, 9-*cis* or 11-*cis* bonds and fixing the rest of the molecule at the initial geometry. Calculated barrier heights relative to the entrance complex (i.e. minimum in the S₁(ππ*) potential energy surface, Fig. 9) are 0.54 eV for the 13-*cis* bond, 0.36 eV for the 9-*cis* bond and 0.29 eV for the 11-*cis* bond. In a semi-classical interpretation, lower photon energies should favour the pathway with the lowest barrier. However, the PISA data [Fig. 4(c)] suggests the opposite: the 9-*cis*:13-*cis* ratio is ≈0.05 at *hv* = 2.8 eV (close to the PISA spectrum onset), ≈0.1 at *hv* = 3.10 eV and ≈0.2 at *hv* = 3.8 eV, indicating a preponderance for the 13-*cis* photoisomer (largest S₁(ππ*) barrier) at lower photon energies. We note that S₁(ππ*) barrier heights for *trans*-RPSB using a relaxed potential energy surface scan are substantially lower (e.g. 0.04 eV for *trans*-RPSB → 11-*cis*-RPSB).[52] Ultimately, the potential energy surface barriers and conical intersections for *trans*-RA⁻ should be recomputed allowing for relaxation of the rest of the molecule. Such calculations are beyond the scope of the present study.

D. Photoisomerisation dynamics in methanol

This section details application of the solution photoisomerisation action (SPISA) spectroscopy technique to provide a comparison between the photoisomerisation properties of *trans*-RA$^-$ in the gas phase and in methanol.

The SPISA spectrum for *trans*-RA$^-$ in methanol is shown in Fig. 10(a). Measurements as function of relative light fluence (see ESI) suggest that one photon causes isomerisation about one double bond, and that 13-*cis* (major, possibly including a small amount of 11-*cis*) and 9-*cis* (minor) are the principal photoisomers. The total SPISA spectrum (*trans* → 13-*cis* + 9-*cis*) closely parallels the absorption spectrum [Fig. 10(a)], which implies that the total photoisomerisation quantum yield is uniform across the absorption band. However, the 9-*cis*:13-*cis* photoisomer branching ratio with photon energy [Fig. 10(b)] shows an inverted trend compared with the gas phase. Specifically, the 9-*cis*:13-*cis* photoisomer branching ratio decreases with photon energy from 0.25 to 0.20 in the 3.0 – 3.5 eV range and plateaus at ≈0.18 for photon energies >3.5 eV. The inversion of the branching ratio in solution compared with the gas-phase is possibly due to solvent-induced modification to the excited state potential energy surfaces, suppression of gas-phase electron detachment processes, and internal energy quenching in solution during the photoisomerisation process.[24, 26, 38-45] It is interesting to note that the *trans*-RA$^-$ solution absorption spectrum, total SPISA spectrum and gas-phase photodepletion spectra [Fig. 4(c)] all have maximum response at 3.70 – 3.85 eV, suggesting there is little solvochromatic shift in the Franck-Condon region.

The lifetimes of the $S_1(\pi\pi^*)$ and $S_3(\pi\pi^*)$ excited states of *trans*-RAH (i.e. the neutral) in solution have been measured previously using several femtosecond spectroscopies. In *n*-hexanol (polar) and *n*-hexane (non-polar) at 298 K, $S_3(\pi\pi^*)$ → $S_1(\pi\pi^*)$ internal conversion occurs on a sub-100 fs timescale[33, 37] (same for $S_2(\pi\pi^*)$ → $S_1(\pi\pi^*)$ internal conversion for β-carotene dissolved in a range of solvents)
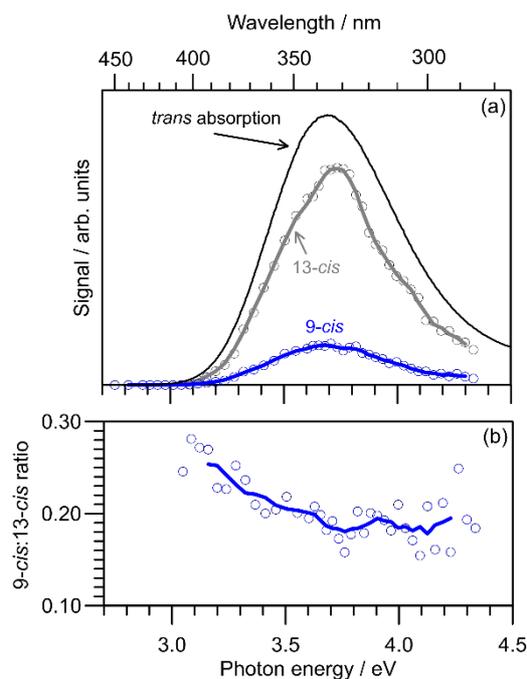

Fig. 10 – (a) SPISA spectra for *trans*-RA$^-$ in pH ≈11 methanol. The total photoisomer signal (13-*cis* + 9-*cis*) closely parallels the solution absorption spectrum (arbitrarily scaled and identical to neutral *trans*-RAH, see ESI), suggesting a uniform total photoisomerisation quantum yield. (b) 9-*cis*:13-*cis* photoisomer ratio with photon energy. Note, a small amount of 11-*cis* might be counted as 13-*cis*.

and does not depend on viscosity.[85, 86] This timescale is roughly the same as the present gas-phase value for *trans*-RA$^-$ presumably because the internal conversion requires little nuclear motion (e.g. only bond stretching). In contrast, the lifetime of the $S_1(\pi\pi^*)$ state of *trans*-RAH in solution depends on solvent polarity and viscosity, surviving for ≈20 ps in *n*-hexane, ≈1.3 ps in methanol and ≈0.9 ps in acetonitrile,[33, 35, 37] with the variation attributed to solvent-specific barriers to isomerisation on the $S_1(\pi\pi^*)$ potential energy surface and possibly changes in isomerisation mechanism, e.g. *trans* → *cis* double bond torsion *vs* a volume conserving hula-twist mechanism. The $S_1(\pi\pi^*)$ lifetime for *trans*-RAH in methanol is approximately six-fold longer than for gas-phase *trans*-RA$^-$ (under the assumption that *trans*-RA$^-$ and *trans*-RAH behave similarly in solution), suggesting that solvation significantly affects the excited state dynamics. Interestingly, a similar situation was predicted some years ago for *trans*-RPSB using direct QM/MM dynamics,[39] which predicted isomerisation timescales comparable with this work: 257±25 fs (gas phase) and 2.8±0.4 ps (explicit shell of methanol molecules). The present *trans*-RA$^-$ measurements should provide a stringent test for QM/MM modelling.

Conclusions

The photoisomerisation and excited state dynamics of gas-phase *trans*-RA$^-$ have been studied using tandem ion mobility spectrometry coupled with laser spectroscopy, and frequency-, angle- and time-resolved photoelectron imaging. The key result from this study is that isolated *trans*-RA$^-$ undergoes a sub-200-fs stereoselective (*trans* → 13-*cis*) photoisomerisation that parallels the dynamics of the retinal protonated Schiff base chromophore in bacteriorhodopsin, despite the absence of protein side-group interactions. This result provides the first experimental verification that ultrafast stereoselective photoisomerisation is an inherent property of *trans*-RA$^-$ and might be a common photochemical property in other similar retinoids. Furthermore, if *trans*-RA$^-$ and retinal protonated Schiff base indeed have similar photoisomerisation dynamics, this study raises new questions on the specific role of the chromophore's binding pocket in opsin proteins (namely bacteriorhodopsin), which has always been thought to facilitate the ultrafast stereoselective photoisomerisation dynamics of the chromophore.

Comparison of the gas-phase measurements on *trans*-RA$^-$ with experiments in methanol using solution photoisomerisation action spectroscopy and femtosecond transient absorption spectroscopy shows that solvation significantly affects the photoisomerisation dynamics in terms of both photoisomer branching with photon energy and the timescale for photoisomerisation. The current results suggest that it is inaccurate to assume an isolated chromophore when computationally modelling dynamics in solution and, perhaps more importantly, solution-based models do not provide an accurate model of the protein environment. The present data should provide baseline measurements for researchers interested in calibrating theory to model how condensed phase environments affect photoisomerisation dynamics.

Finally, the experimental strategy of combining data sets from ion mobility spectrometry and time-resolved photoelectron spectroscopy is well suited for investigating the photophysics in a wide range of other photoisomerising anions, including stilbene chromophores in molecular photoswitches and deprotonated *para*-coumaric acids as models for the chromophore in photoactive yellow protein. These examples will be presented in forthcoming studies.

Acknowledgements

Conflicts of interest

There are no conflicts to declare.

Author contributions

Ion mobility experiments were performed by JNB in the laboratory of EJB. Photoelectron experiments were performed by JNB, CWW and CSA in the laboratory of JRRV. Electronic structure calculations were performed by JNB, and RRKM theory modelling was performed by GdS. The manuscript was prepared by JNB.

References

1. K. L. Pierce, R. T. Premont and R. J. Lefkowitz, *Nat. Rev. Mol. Cell Biol.*, 2002, **3**, 639-650.
2. O. P. Ernst, D. T. Lodowski, M. Elstner, P. Hegemann, L. S. Brown and H. Kandori, *Chem. Rev.*, 2014, **114**, 126-163.
3. J. L. Spudich, C.-S. Yang, K.-H. Jung and E. N. Spudich, *Ann. Rev. Cell Dev. Biol.*, 2000, **16**, 365-392.
4. Y. Shichida and T. Matsuyama, *Phil. Trans. Royal Soc. London B: Biol. Sci.*, 2009, **364**, 2881-2895.
5. G. Wald, *Science*, 1968, **162**, 230-239.
6. R. Schoenlein, L. Peteanu, R. Mathies and C. Shank, *Science*, 1991, **254**, 412-415.
7. J. Herbst, K. Heyne and R. Diller, *Science*, 2002, **297**, 822-825.
8. D. Polli, P. Altoe, O. Weingart, K. M. Spillane, C. Manzoni, D. Brida, G. Tomasello, G. Orlandi, P. Kukura, R. A. Mathies, M. Garavelli and G. Cerullo, *Nature*, 2010, **467**, 440-443.
9. P. J. M. Johnson, A. Halpin, T. Morizumi, V. I. Prokhorenko, O. P. Ernst and R. J. D. Miller, *Nat. Chem.*, 2015, **7**, 980-986.
10. K. C. Hasson, F. Gai and P. A. Anfinrud, *Proc. Nat. Acad. Sci.*, 1996, **93**, 15124-15129.
11. T. Kobayashi, T. Saito and H. Ohtani, *Nature*, 2001, **414**, 531-534.
12. J. Tittor and D. Oesterhelt, *FEBS Letters*, 1990, **263**, 269-273.
13. J. E. Kim, M. J. Tauber and R. A. Mathies, *Biochem.*, 2001, **40**, 13774-13778.
14. S. Gozem, H. L. Luk, I. Schapiro and M. Olivucci, *Chem. Rev.*, 2017, **117**, 13502-13585.
15. M. Ben-Nun, F. Molnar, K. Schulten and T. J. Martínez, *Proc. Nat. Acad. Sci.*, 2002, **99**, 1769-1773.
16. C. Schnedermann, M. Liebel and P. Kukura, *J. Am. Chem. Soc.*, 2015, **137**, 2886-2891.
17. E. Nango, A. Royant, M. Kubo, T. Nakane, C. Wickstrand, T. Kimura, T. Tanaka, K. Tono, C. Song, R. Tanaka, T. Arima, A. Yamashita, J. Kobayashi, T. Hosaka, E. Mizohata, P. Nogly, M. Sugahara, D. Nam, T. Nomura, T. Shimamura, T. Im, T. Fujiwara, Y. Yamanaka, B. Jeon, T. Nishizawa, K. Oda, M. Fukuda, R. Andersson, P. Båth, R. Dods, J. Davidsson, S. Matsuoka, S. Kawatake, M. Murata, O. Nureki, S. Owada, T. Kameshima, Y. Hatsui, Y. Joti, G. Schertler, M. Yabashi, A.-N. Bondar, J. Standfuss, R. Neutze and S. Iwata, *Science*, 2016, **354**, 1552-1557.
18. P. Nogly, T. Weinert, D. James, S. Carbajo, D. Ozerov, A. Furrer, D. Gashi, V. Borin, P. Skopintsev, K. Jaeger, K. Nass, P. Båth, R. Bosman, J. Koglin, M. Seaberg, T. Lane, D. Kekilli, S. Brünle, T. Tanaka, W. Wu, C. Milne, T. White, A. Barty, U. Weierstall, V. Panneels, E. Nango, S. Iwata, M. Hunter, I. Schapiro, G. Schertler, R. Neutze and J. Standfuss, *Science*, 2018, **361**, eaat0094.
19. P. D. Kiser, M. Golczak and K. Palczewski, *Chem. Rev.*, 2014, **114**, 194-232.
20. J. L. Napoli, *Biochim. Biophys. Acta*, 2012, **1821**, 152-167.
21. *Carotenoids in Nature: Biosynthesis, Regulation and Function*, Springer, 2016.
22. V. Laudet, E. Zieger and M. Schubert, eds. P. Dollé and K. Neiderreither, John Wiley & Sons, Inc., Hoboken, NJ, 2015, ch. 4. Evolution of the Retinoic Acid Signaling Pathway, pp. 75-90.
23. D. Kirilovsky and C. A. Kerfeld, *Nat. Plants*, 2016, **2**, 16180.
24. G. Zgrablić, A. M. Novello and F. Parmigiani, *J. Am. Chem. Soc.*, 2012, **134**, 955-961.
25. G. Bassolino, T. Sovdat, A. S. Duarte, J. M. Lim, C. Schnedermann, M. Liebel, B. Odell, T. D. W. Claridge, S. P. Fletcher and P. Kukura, *J. Am. Chem. Soc.*, 2015, **137**, 12434-12437.
26. G. Zgrablić, M. Ricci, A. M. Novello and F. Parmigiani, *Photochem. Photobiol.*, 2010, **86**, 507-512.
27. R. S. Becker and K. Freedman, *J. Am. Chem. Soc.*, 1985, **107**, 1477-1485.
28. K. A. Freedman and R. S. Becker, *J. Am. Chem. Soc.*, 1986, **108**, 1245-1251.
29. S. L. Logunov, L. Song and M. A. El-Sayed, *J. Phys. Chem.*, 1996, **100**, 18586-18591.
30. T. Sovdat, G. Bassolino, M. Liebel, C. Schnedermann, S. P. Fletcher and P. Kukura, *J. Am. Chem. Soc.*, 2012, **134**, 8318-8320.
31. G. Zgrablić, K. Voïtchovsky, M. Kindermann, S. Haacke and M. Chergui, *Biophys. J.*, 2005, **88**, 2779-2788.
32. M. R. V. Sahun and N. Serpone, *J. Photochem. Photobiol. A: Chem.*, 1998, **115**, 231-238.
33. L. Zhang, J. Yang, L. W. W.-Z. Yang and Y.-X. Weng, *J. Chem. Phys. B*, 2003, **107**, 13688-13697.
34. J. Xiang, F. S. Rondonuwu, Y. Kakitani, R. Fujii, Y. Watanabe, Y. Koyama, H. Nagae, Y. Yamano and M. Ito, *J. Phys. Chem. B*, 2005, **109**, 17066-17077.
35. I. Presiado, S. Shomer, Y. Erez, R. Gepshtein, N. Amdursky and D. Huppert, *J. Photochem. Photobiol. A: Chem.*, 2013, **258**, 30-40.
36. M. G. Vivas, J. P. Siqueira, D. L. Silva, L. de Boni and C. R. Mendonca, *RSC Adv.*, 2015, **5**, 74531-74538.
37. O. Flender, M. Scholz, J. Holzer, K. Oum and T. Lenzer, *Phys. Chem. Chem. Phys.*, 2016, **18**, 14941-14948.
38. A. Muñoz-Losa, M. E. Martín, I. F. Galvan, M. L. Sanchez and M. A. Aguilar, *J. Chem. Theory Comput.*, 2011, **7**, 4050-4059.
39. C. Punwong, J. Owens and T. J. Martínez, *J. Phys. Chem. B*, 2015, **119**, 704-714.
40. L. Liu, J. Liu and T. J. Martínez, *J. Phys. Chem. B*, 2015, **120**, 1940-1949.
41. I. Burghardt, L. S. Cederbaum and J. T. Hynes, *Faraday Discuss.*, 2004, **127**, 395-411.

42. G. Zgrablić, S. Haacke and M. Chergui, *J. Phys. Chem. B*, 2009, **113**, 4384-4393.
43. J. P. Malhado and J. T. Hynes, *J. Chem. Phys.*, 2012, **137**, 15.
44. J. P. Malhado, R. Spezia and J. T. Hynes, *J. Phys. Chem. A*, 2011, **115**, 3720-3735.
45. M. Manathunga, X. Yang, Y. Orozco-Gonzalez and M. Olivucci, *J. Phys. Chem. Lett.*, 2017, **8**, 5222-5227.
46. L. H. Andersen, I. B. Nielsen, M. B. Kristensen, M. O. A. El Ghazaly, S. Haacke, M. B. Nielsen and M. Å. Petersen, *J. Am. Chem. Soc.*, 2005, **127**, 12347-12350.
47. I. B. Nielsen, L. Lammich and L. H. Andersen, *Phys. Rev. Lett.*, 2006, **96**, 018304.
48. J. Rajput, D. Rahbek, L. Andersen, A. Hirshfeld, M. Sheves, P. Altoe, G. Orlandi and M. Garavelli, *Angew. Chem., Int. Ed.*, 2010, **49**, 1790-1793.
49. O. Valsson and C. Filippi, *J. Phys. Chem. Lett.*, 2012, **3**, 908-912.
50. N. J. A. Coughlan, K. J. Catani, B. D. Adamson, U. Wille and E. J. Bieske, *J. Chem. Phys.*, 2014, **140**, 164307.
51. N. J. A. Coughlan, B. D. Adamson, L. Gamon, K. Catani and E. J. Bieske, *Phys. Chem. Chem. Phys.*, 2015, **17**, 22623-22631.
52. H. V. Kiefer, E. Gruber, J. Langeland, P. A. Kusochek, A. V. Bochenkova and L. H. Andersen, *Nature Communications*, 2019, **10**.
53. J. N. Bull, M. S. Scholz, E. Carrascosa, G. da Silva and E. J. Bieske, *Phys. Rev. Lett.*, 2018, **120**, 223002.
54. J. N. Bull, C. W. West and J. R. R. Verlet, *Chem. Sci.*, 2015, **6**, 1578-1589.
55. B. D. Adamson, N. J. A. Coughlan, P. B. Markworth, R. E. Continetti and E. J. Bieske, *Rev. Sci. Instr.*, 2014, **85**, 123109.
56. J. N. Bull, E. Carrascosa, N. Mallo, M. S. Scholz, G. da Silva, J. E. Beves and E. J. Bieske, *J. Phys. Chem. Lett.*, 2018, **9**, 665-671.
57. J. N. Bull, E. Carrascosa, Giacomozzi, L., E. J. Bieske and M. H. Stockett, *Phys. Chem. Chem. Phys.*, 2018, **20**, 19672-19681.
58. J. N. Bull, E. Carrascosa, M. S. Scholz, N. J. A. Coughlan and E. J. Bieske, *Analyst*, 2017, **142**, 2100-2103.
59. D. A. Horke, G. M. Roberts, J. Lecointre and J. R. R. Verlet, *Rev. Sci. Instrum.*, 2012, **83**, 062101.
60. G. M. Roberts, J. L. Nixon, J. Lecoitre, E. Wrede and J. R. R. Verlet, *Rev. Sci. Instrum.*, 2009, **80**, 053104.
61. R. N. Zare, *Mol. Photochem.*, 1972, **4**, 1-37.
62. J. N. Bull, C. W. West and J. R. R. Verlet, *Phys. Chem. Chem. Phys.*, 2015, **17**, 32464-32471.
63. A. A. Granovsky, *Firefly version 8.2.0, http://classic.chem.msu.su/gran/firefly/index.html*.
64. F. Neese, *WIRES Comp. Mol. Sci.*, 2012, **2**, 73.
65. M. J. Frisch, G. W. Trucks, H. B. Schlegel, G. E. Scuseria, M. A. Robb, J. R. Cheeseman, G. Scalmani, V. Barone, G. A. Petersson, H. Nakatsuji, X. Li, M. Caricato, A. V. Marenich, J. Bloino, B. G. Janesko, R. Gomperts, B. Mennucci, H. P. Hratchian, J. V. Ortiz, A. F. Izmaylov, J. L. Sonnenberg, D. Williams-Young, F. Ding, F. Lipparini, F. Egidi, J. Goings, B. Peng, A. Petrone, T. Henderson, D. Ranasinghe, V. G. Zakrzewski, J. Gao, N. Rega, G. Zheng, W. Liang, M. Hada, M. Ehara, K. Toyota, R. Fukuda, J. Hasegawa, M. Ishida, T. Nakajima, Y. Honda, O. Kitao, H. Nakai, T. Vreven, K. Throssell, J. J. A. Montgomery, J. E. Peralta, F. Ogliaro, M. J. Bearpark, J. J. Heyd, E. N. Brothers, K. N. Kudin, V. N. Staroverov, T. A. Keith, R. Kobayashi, J. Normand, K. Raghavachari, A. P. Rendell, J. C. Burant, S. S. Iyengar, J. Tomasi, M. Cossi, J. M. Millam, M. Klene, C. Adamo, R. Cammi, J. W. Ochterski, R. L. Martin, K. Morokuma, O. Farkas, J. B. Foresman and D. J. Fox, *Gaussian 16 Revision B.01*, Gaussian, Inc., Wallingford CT, 2016.
66. A. D. Becke, *J. Chem. Phys.*, 1993, **98**, 1372-1377.
67. T. H. Dunning, *J. Chem. Phys.*, 1989, **90**, 1007.
68. C. Riplinger, C. B. Sandhoefer, C. B. A. Hansen and F. Neese, *J. Chem. Phys.*, 2013, **139**, 134101.
69. Z. Fu, X. Li and K. M. Merz Jr., *J. Chem. Theory Comput.*, 2012, **8**, 1436-1448.
70. B. D. Cox, D. D. Muccio and T. P. Hamilton, *Comput. Theor. Chem.*, 2013, **1011**, 11-20.
71. A. A. Granovsky, *J. Chem. Phys.*, 2011, **134**, 214113.
72. I. Campuzano, M. F. Bush, C. V. Robinson, C. Beaumont, K. Richardson, H. Kim and H. I. Kim, *Anal. Chem.*, 2012, **84**, 1026-1033.
73. B. H. Besler, J. Merz, K. M. and P. A. Kollman, *J. Comp. Chem.*, 1990, **11**, 431.
74. J. R. Barker, T. L. Nguyen, J. F. Stanton, C. Aieta, M. Ceotto, F. Gabas, T. J. D. Kumar, C. G. L. Li, L. L. Lohr, A. Maranzana, N. F. Ortiz, J. M. Preses, J. M. Simmie, J. A. Sonk and P. J. Stimac, *Multiwell-2017 Software Suite: http://clasp-research.engin.umich.edu/multiwell/*, University of Michigan, 2017.
75. J. N. Bull, M. S. Scholz, N. J. A. Coughlan, A. Kawai and E. J. Bieske, *Anal. Chem.*, 2016, **88**, 11978-11981.
76. R. W. Curley, Jr. and J. W. Fowble, *Photochem. Photobiol.*, 1988, **47**, 831-835.
77. D. K. Bempong, I. L. Honigberg and N. M. Meltzer, *J. Pharm. Biomed. Anal.*, 1995, **13**, 285-291.
78. M. G. Motto, K. L. Facchine, P. F. Hamburg, D. J. Burinsky, R. Dunphy, A. R. Oyler and M. L. Cotter, *J. Chromat.*, 1989, **481**, 255-262.
79. A. R. Sundquist, W. Stahl, A. Steigel and H. Sies, *J. Chromat. A*, 1993, **637**, 201-205.
80. S. T. Graul and R. R. Squires, *J. Am. Chem. Soc.*, 1988, **110**, 607-608.
81. J. Gidden and M. Bowers, *J. Am. Chem. Mass Spectrom.*, 2003, **14**, 161-170.
82. J. N. Bull, C. W. West and J. R. R. Verlet, *Chem. Sci.*, 2016, **7**, 5352-5361.
83. J. N. Bull and J. R. R. Verlet, *Sci. Adv.*, 2017, **3**, e1603106.
84. D. J. Nesbitt and R. W. Field, *J. Phys. Chem. A*, 1996, **100**, 12735.
85. A. N. Macpherson and T. Gillbro, *J. Phys. Chem. A*, 1998, **102**, 5049-5058.
86. M. Liebel, C. Schnedermann and P. Kukura, *Phys. Rev. Lett.*, 2014, **112**, 198302.